Filtering for distributed mechanical systems using position measurements: perspectives in medical imaging

Philippe Moireau, Dominique Chapelle, Patrick Le Tallec

Filtering for distributed mechanical systems using position measurements: Perspectives in medical imaging

Philippe Moireau†,* Dominique Chapelle†, Patrick Le Tallec‡
†INRIA, B.P. 105, 78153 Le Chesnay cedex, France
‡Ecole Polytechnique, 91128 Palaiseau cedex, France

Inverse Problems, 25(3), 2009, doi:10.1088/0266-5611/25/3/035010

Abstract

We propose an effective filtering methodology designed to perform estimation in a distributed mechanical system using position measurements. As in a previously introduced method, the filter is inspired from robust control feedback, but here we take full advantage of the estimation specificity to choose a feedback law that can act on displacements instead of velocities and still retain the same kind of dissipativity property which guarantees robustness. This is very valuable in many applications for which positions are more readily available than velocities, as in medical imaging. We provide an in-depth analysis of the proposed procedure, as well as detailed numerical assessments using a test problem inspired from cardiac biomechanics, as medical diagnosis assistance is an important perspective for this approach. The method is formulated first for measurements based on Lagrangian displacements, but we then derive a nonlinear extension allowing to instead consider segmented images, which of course is even more relevant in medical applications.

1 Introduction

Estimation by filtering – e.g. Kalman filtering – has long been restricted to dynamical systems limited in size, due to the costs induced by the computation of the filter, both in terms of storage and CPU time. In particular, although it can be formulated in theory [5] optimal filtering for partial differential equations (PDEs) gives rise to untractable computations in practice, when considering discretized versions of the system. Only recently have some so-called "reduced-rank filtering procedures" been proposed in the data assimilation community in order to deal with such large systems by reducing the size of the space of "uncertain variables" considered [18]. However, in many infinite dimensional systems – such as the class of mechanical systems considered here – this uncertainty space is *intrinsically* very large, hence generic rank reduction is not applicable.

In [14] we have proposed a filtering methodology well-adapted to evolution PDEs, in which the filter is inspired from feedback control concepts and Luenberger observers [13]. In mechanics, in particular, collocated feedback is known to provide robust – as can also be mathematically substantiated – and easily implementable control laws for large classes of systems. When taking the feedback operator as a filter, it can be shown for linear systems that the estimation error obeys the closed-loop dynamics associated with this feedback, hence enjoys the same convergence properties. This holds for state estimation, but it can be extended to joint state-parameter estimation by using this state filter in essence to "reduce the uncertainty" to the parameter space, and take advantage ot

*Corresponding author: philippe.moireau@inria.fr

the reduced uncertainty to formulate the joint estimation problem in an H^2-optimal or H^∞-robust framework [14, 6].

We have also discussed how this type of approach has perspectives in medical diagnosis assistance, as the combination of information provided by measurements – namely signals and images – on the one hand, and by various physical and physiological models on the other hand, when adequately processed by estimation procedures to produce meaningful and accurate medical indicators, may be of utmost value [2]. When more specifically considering biomechanical modelling an important application field for such data assimilation methodologies is cardiology [22], for which quantitative mechanical indicators are most relevant, and also pneumology to some extent [25].

Nevertheless, a limitation of our approach in mechanical systems is that collocated feedbacks use velocity measurements – hence so does the corresponding filter – whereas such measurements are not always readily available. In most cases – e.g. in medical imaging – position measurements are much easier to obtain. In fact, in imaging the measurement gives a snapshot of the deformed configuration along time, which does not directly provide an access to the Lagrangian displacements, hence induces a very serious additional difficulty. And even when displacements are directly available – as may be the case after postprocessing specific imaging modalities such as tagged MRI – differentiating them to obtain velocities for the filtering procedure is of course not recommended, as it considerably amplifies the various measurement errors.

However, this limitation can be lifted by taking fuller advantage of our approach of devising a filter based on feedback laws, when noting that in our case we only need to apply the control on a *numerical system* – not on the real one. Hence, although we are limited on the sensor operator that can be used in the control law and that must correspond to the actual measurements available for the system, we have much more freedom on the actuator side. In particular, the control can apply on the equation relating displacement and velocity when writing the dynamical system in the usual first-order form, whereas this type of actuation cannot be considered for a real system. In this paper, we show that this idea allows to use displacement measurements with the same effectiveness as for velocities in [14]. Furthermore we demonstrate how this can be extended to consider position snapshots, as available in segmented images.

The outline of the article is as follows. In Section 2 we define the model setting and introduce the notation. Then, in Section 3 we present our new filtering approach, starting with measurements that contain only Lagrangian displacements – namely, the essential unknowns in the mechanical system – for various types of observation operators: displacements integrated over 3D measurement cells, boundary displacements, and boundary-normal displacements. We analyse this estimation procedure both mathematically and numerically – by computing the poles of the associated closed-loop dynamics – and we also demonstrate its performance by computing the estimation error in a test problem inspired from cardiac biomechanics. We next proceed to extend this approach in Section 4, in order to be able to use the – intrisically Eulerian – position information available in segmented images. As the filter formulation was introduced in the framework of linear mechanical systems, we also present in Section 5 a natural extension of the approach for nonlinear mechanics, with a numerical assessment. Finally we give some concluding remarks in Section 6.

2 Problem statement

2.1 General Framework

We consider a mechanical system in the realm of solid or structural continuum mechanics, where the acceleration field inside the body is given by the imbalance between internal stresses and external forces. When x denotes the state vector including displacements $\underline{y}$ and velocities $\underline{\dot{y}}$, such systems are described in a linear framework by a dynamical system – underlied by partial differential equations

– written in the following generic form

$$\begin{cases} \dfrac{dx}{dt} = \mathcal{A}x + \mathcal{R} \\ x(0) = x_0 + \zeta_x \end{cases} \tag{1}$$

where $\mathcal{A}$ is a linear differential operator and $\mathcal{R}$ a source term. More specifically, this equation expresses the conservation of linear momentum, completed by the identity relating the velocity and the time derivative of displacement, namely, in a weak form,

$$\int_\Omega \rho \frac{d\underline{\dot{y}}}{dt} \cdot \delta\underline{y}\, d\Omega = \int_\Omega \rho \underline{\dot{y}} \cdot \delta\underline{y}\, d\Omega, \quad \forall \delta\underline{y} \tag{2}$$

$$\int_\Omega \rho \frac{d\underline{\dot{y}}}{dt} \cdot \delta\underline{y}\, d\Omega = -\int_\Omega \underline{\underline{\Sigma}}(\underline{y}, \underline{\dot{y}}) : \delta\underline{\underline{e}}\, d\Omega + \int_\Omega \underline{f} \cdot \delta\underline{y}\, d\Omega, \quad \forall \delta\underline{y} \tag{3}$$

Here, Ω represents the geometrical domain of the system, ρ the mass per unit volume, $\underline{\underline{\Sigma}}$ the second Piola-Kirchhoff stress tensor, $\delta\underline{y}$ an arbitrary test function in the displacement space with $\delta\underline{\underline{e}}$ the corresponding infinitesimal variation for the Green-Lagrange strain tensor, and $\underline{f}$ the applied loading (taken here as a 3D distributed field to fix the ideas). Hence, in System (1) x denotes the state variable $\begin{pmatrix} \underline{y} & \underline{\dot{y}} \end{pmatrix}^T$. Assuming *small displacements*, we can identify $\delta\underline{\underline{e}}$ with the symmetric part of the gradient $\nabla\delta\underline{y}$, and take $\underline{\underline{\Sigma}}$ – which can then be identified with the Cauchy stress tensor – as a linear function of x. We are thus led to the *linear* operator $\mathcal{A}$. The differential system considered is of infinite dimension, its unknowns being the displacement and velocity fields at each point of the continuous body.

In the above system, ζ_x represents the unknown part in the initial condition $x(0)$. Our objective is to obtain an estimation of the unknown quantities ζ_x , based on measurements available for the system.

Let us introduce A and R as the discrete counterparts of $\mathcal{A}$ and $\mathcal{R}$ obtained from a finite element approximation of the variational formulation, namely,

$$A = \begin{pmatrix} 0 & I \\ -M^{-1}K & -M^{-1}C \end{pmatrix}, \quad R = \begin{pmatrix} 0 \\ M^{-1}F \end{pmatrix}, \tag{4}$$

where M, C, K and F respectively denote the mass, damping and stiffness matrices and the consistent force vector, see [4, 11]. The discrete space variable $X \in \mathbb{R}^N$ thus satisfies the dynamical system

$$\begin{cases} \dot{X} = AX + R \\ X(0) = X_0 + \zeta_X \end{cases} \tag{5}$$

where X_0 and ζ_X are discrete approximations – typically by interpolation – of x_0 and ζ_x.

Our final objective consists in finding a procedure to approximate the real system with the finite element model without knowing the corresponding approximation of ζ_X, but using the available measurements.

2.2 Model Problem

In order to illustrate and assess our estimation procedures, we will consider an example problem inspired from biomechanics and representing a simplified cardiac ventricle. This model problem was already considered in [14], but for completeness we now summarize its definition.

The geometry of our example problem is depicted in Figure 1-(a), and the characteristic dimensions of this object are – indeed – comparable to those of a human left ventricle. We thus resort to cardiac

terminology to refer to the two extremities of the object, namely "apex and base" (see Figure). The system is clamped over the planar surface at the base, and activated by a spherical wave of prestress – representing electrical activation – of initiation center C and wave speed $c = 0.5$ m.s^{-1}, which means that it takes 0.2 s for the wave to reach the base. The wave shape itself is shown in Figure 2. The resulting prestress state is assumed to be isotropic and gives an external virtual work defined by

$$\delta\mathcal{W}^{PS} = \int_\Omega \sigma_0 w(\|\underline{CM}\| - ct)\ \mathrm{Tr}(\delta\nabla\underline{y})\, d\Omega = \delta Y^T \cdot R, \tag{6}$$

Our simulations will correspond to an isotropic viscoelastic material in *linear analysis*, with material parameters given by

$$E = 12.4\,10^3\,\mathrm{Pa}, \quad \nu = 0.39, \quad \eta = 1.6\,10^{-4}\,\mathrm{s}, \quad \sigma_0 = 4.5\,10^4\,\mathrm{Pa}, \tag{7}$$

and respectively denoting Young's modulus, the Poisson ratio and a viscoelastic relaxation time associated with the pseudo-potential

$$W^v = \eta\left(\frac{\lambda}{2}(\mathrm{Tr}\,\underline{\underline{\dot\varepsilon}})^2 + \mu\,\mathrm{Tr}(\underline{\underline{\dot\varepsilon}}^2)\right),$$

where λ et μ are the Lamé constants derived from E and ν, and

$$\underline{\underline{\varepsilon}} = \frac{1}{2}\big(\nabla\underline{y}^T + \nabla\underline{y}\big)$$

denotes the linearized strain tensor approximating – at the first order – the Green-Lagrange deformation tensor in the small displacements framework. Note that this viscoelastic contribution corresponds to stiffness-based Rayleigh proportional damping. This leads to the following constitutive law to be taken into account in the variational formulation

$$\underline{\underline{\Sigma}} = \lambda\,\mathrm{Tr}(\underline{\underline{\varepsilon}} + \eta\underline{\underline{\dot\varepsilon}})\underline{\underline{1}} + 2\mu(\underline{\underline{\varepsilon}} + \eta\underline{\underline{\dot\varepsilon}}). \tag{8}$$

Also, volumic mass is set as $\rho = 10^3\,\mathrm{kg}\cdot\mathrm{m}^{-3}$, a standard value for biological tissues. All these material parameter values are taken in consistency with [20] and lead to physiological heart functional indicators in the simulations. Note that – unless otherwise stated – all physical units implicitly correspond to the SI system.

For practical purposes, in our test problem the "real system" is given by a finite element model associated with a mesh much finer than the computational meshes that we want to use for the estimation. This reference mesh is displayed in Figure 1-(b) and features nearly 40000 degrees of freedom. As seen in the figure, this corresponds to a fine mesh, with typically about 10 elements across the thickness of the wall, and it can be checked that it provides a numerically converged solution. Therefore, the measurements used in the estimation will be synthesized using the simulations of this reference model and adding some realistic measurement noise. In our simulations we will consider two types of uncertainties:

1. random (Gaussian) errors, generated independently for each node of the reference mesh, for each component of the displacement and for each time step, and with standard deviation set to 20% of the reference maximum displacement value $d_{\max}$;

2. modal shift, namely, a displacement profile corresponding to the trace of the first undamped eigenmode and constant in time, with an amplitude computed to give 20% of the strain energy norm of a constant displacement field equal to $d_{\max}$ for each component.

Note that these error amplitudes are quite large, as $d_{\max}$ is an upper bound of the displacement value. The total energy – namely, the sum of strain and kinetic energies – and the cavity volume for the reference solution are shown in Figure 2, as classical indicators of the mechanical and physiological behavior. The observer itself will be based on the coarser discretization displayed in Figure 1-(c) with about 6000 degrees of freedom, which is chosen to give discretization errors consistent with the measurement errors, hence with the level of accuracy actually sought in the estimation procedure. In all our simulations we used for time discretization the energy-conserving Newmark algorithm with time step $\Delta t = 1\,\text{ms}$ [4, 12]. This time step is adequate for accurately representing the first 1000 eigenmodes of the system with at least 20 time steps per modal period, but is primarily determined in relation to the activation wave velocity. Hence, as regards spectral and dynamical stability properties this corresponds to an "overkill" discretization strategy, as we do not analyse the effect of time step sizes in this paper, which of course would also be worthy of investigation [9].

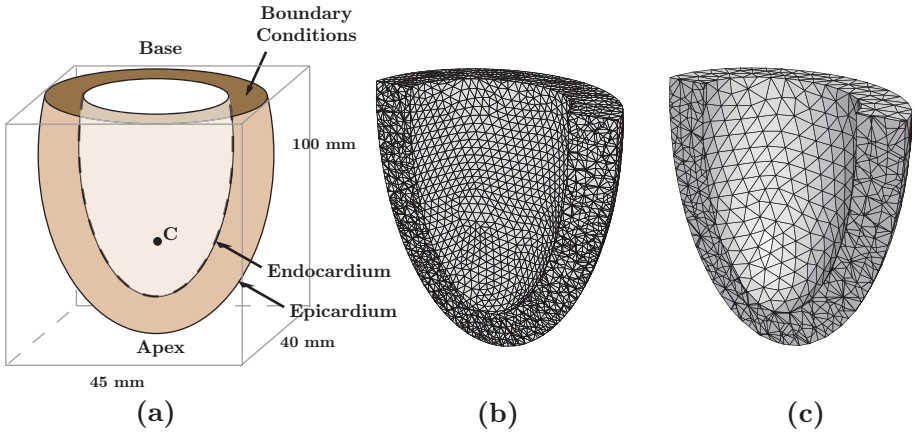

Figure 1: (a) model geometry – (b) reference mesh – (c) observer mesh

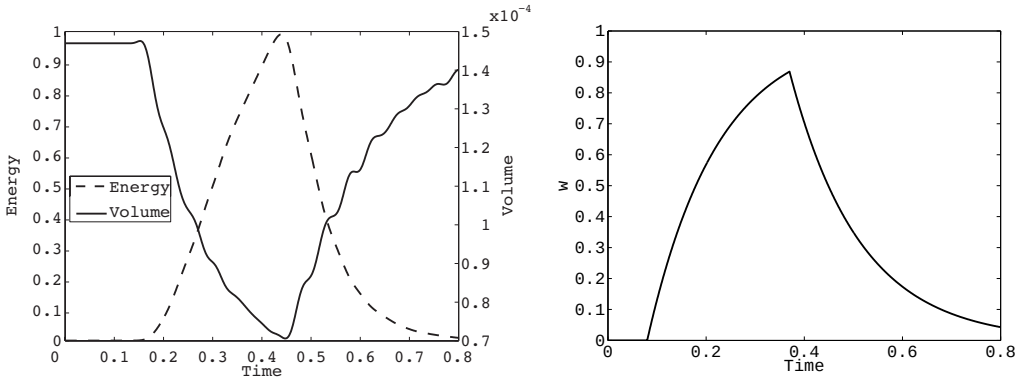

Figure 2: Energy and volume of the cavity for the reference solution (left)– Electrical activation profile (right)

3 Estimation from Lagrangian displacement measurements

3.1 Collocated state estimator

In this section, we begin by assuming that the measurements are given by

$$Z = \mathcal{H}x + \chi,$$

where $\mathcal{H}$ is a linear operator referred to as the observation operator, and χ denotes an error introduced by the measurement procedure (detection, sampling...). We also introduce the corresponding spacewise-discrete observation operator

$$H = \mathcal{H} \circ \mathcal{I}_h, \tag{9}$$

where $\mathcal{I}_h$ denote the one-to-one mapping from the space of degrees of freedom to the state space, so that

$$\bar{Z} = HX + \chi + \epsilon_h, \tag{10}$$

with $\epsilon_h = \mathcal{H}(x - \mathcal{I}_h X)$ the image of the discretization error in the observation space, namely, a "small term" which can be decreased by refining the mesh.

In this section we assume that the measurements are a continuous function of the displacement field. This occurs for example in the case of displacement extraction from tagged MRI [8]. As described in [14], we can formalize this reconstructed field based on tagged MRI data as displacements sampled in space using weight functions $(s_i)_{i=1}^q$ defined on q non-overlapping "measurement cells" within Ω_m. Namely, $\mathcal{H}x = (\mathcal{H}^d \ 0)(\underline{y} \ \underline{\dot{y}})^T$ then consists of the q three-dimensional vectors given by

$$\int_{\Omega_m} s_i \, \underline{y} \, d\Omega,$$

and we assume that the sampling functions are normalized, i.e. $\|s_i\|_{L^2(\Omega_m)} = 1$. In the simulations to come, the cells are defined by subdividing a (rectangular) box enclosing the geometry into $10 \times 10 \times 15$ smaller (rectangular) cells of equal sizes. This subdivision is visualized in Figure 3[1]. The weight functions are then simply defined by scaled indicator functions of the cells. We point out that this resolution is comparable to that of standard tagged MRI images.

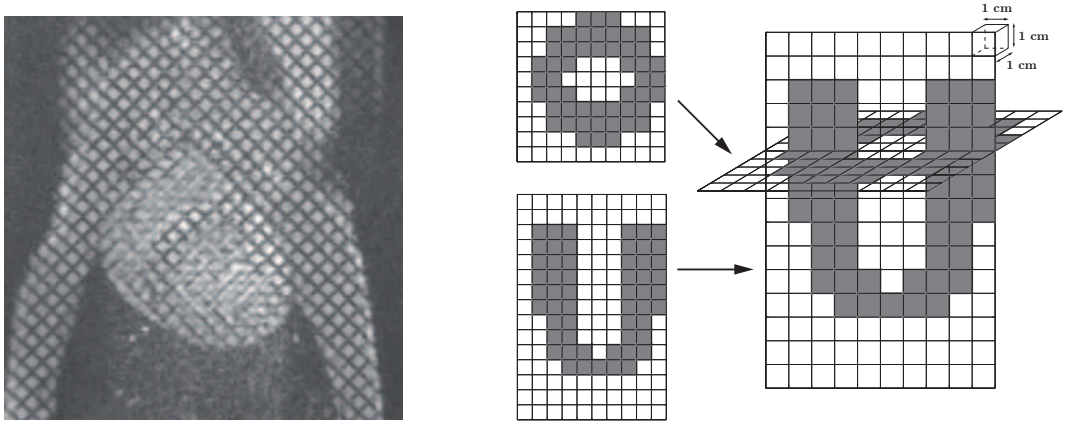

Figure 3: Tagged MRI (left) – Measurement cells in synthetic data (right)

[1]Tagged MRI image is courtesy J. Garot (Henri Mondor Hospital - Créteil - France)

Our goal is to find a filter operator K_X such that the following state estimator

$$\begin{cases} \dot{\hat{X}} = A\hat{X} + R + K_X(Z - H\hat{X}) \\ \hat{X}(0) = X_0 \end{cases} \tag{11}$$

converges to the real system. In other words, for linear systems we expect that the state estimation error

$$\tilde{X} = X - \hat{X},$$

$$\begin{cases} \dot{\tilde{X}} = (A - K_X H)\tilde{X} - K_X(\chi + \epsilon_h) \\ \tilde{X}(0) = \zeta_X \end{cases} \tag{12}$$

converges to a "small value" in a much shorter time than the characteristic simulation window.

Note that in practice, continuous time measurements are never available, so we need to take into account time sampling for the data Z. Assuming that we only have $Z_k = Z(k\Delta T),\ 1 \leq k \leq N_{\Delta T}$ – with ΔT the measurement time step – we define the reconstructed time continuous measurement Z_{int} by interpolation, e.g. with the linear formula

$$Z_{\text{int}} = \alpha_k(t)Z_k + (1 - \alpha_k(t))Z_{k+1}, \text{ with } \alpha_k(t) = \tfrac{(k+1)\Delta T - t}{\Delta T}.$$

In this case, we substitute Z_{int} for Z in (11) and this leads to the modified error equation

$$\dot{\tilde{X}} = (A - K_X H)\tilde{X} - K_X(\chi + \epsilon_h + (Z_{\text{int}} - Z)),$$

where $Z_{\text{int}} - Z$ is an interpolation error of order $O(\Delta T)$. For the sake of compactness we will omit this additional error term in our forthcoming mathematical derivations, but we will use interpolated measurements in Section 4.

We have already presented in [14] some state estimators based on velocity measurements where a simple "direct velocity feedback" (DVF) strategy directly leads to a dissipative operator in the error system (12). This consists in using velocity measurements to correct the observer dynamics by applying forces proportional to the discrepancy with the observer velocity at the same locations. In feedback control – from which our method was directly inspired – this corresponds to *collocated* sensors and actuators [19]. Note that, in order to be directly dissipative, the control (a force) needs to be dual to the sensing (a velocity) from the mechanical energy point of view. Here, the measurements concern displacements and no longer velocities. This difference requires a modification of our stabilization strategy because a "DVF-like" displacement feedback will not directly induce the decrease of the estimation error, but instead increase the rigidity of this system. Namely, if we define as in [14]

$$K_X = \begin{pmatrix} 0 \\ \gamma M^{-1}(H^d)' \end{pmatrix}, \tag{13}$$

with γ a gain coefficient to be adjusted in the feedback, setting $\hat{X} = (\hat{Y}\ \dot{\hat{Y}})^T$ we have the second order dynamics

$$M\ddot{\hat{Y}} + C\dot{\hat{Y}} + \big(K + \gamma(H^d)'H^d\big)\hat{Y} = R + \gamma(H^d)'Z, \tag{14}$$

where the rigidity K is increased with the positive operator $\gamma(H^d)'H^d$. As a matter of fact, in systems where natural damping is an increasing function of the frequency – e.g. for stiffness proportional damping – this additional stiffness induces at the first order an increase in the modal damping, albeit only indirectly.

The DVF strategy was already inspired from control techniques, but since the estimator is a numerical system we emphasize that we are free to modify the dynamics in any suitable way.

Then we choose to modify the first equation (2) giving the velocity as the differentiation of the displacement, instead of the second equation (3) as in (13)-(14). In the discrete estimator system we thus define

$$K_X = \begin{pmatrix} \gamma K^{-1}(H^d)' \\ 0 \end{pmatrix}, \tag{15}$$

so that the system becomes, for $\hat{X} = (\hat{X}^d\ \hat{X}^v)^T$,

$$\begin{cases} K\dot{\hat{X}}^d = K\hat{X}^v + \gamma(H^d)'(Z - H^d\hat{X}^d) \\ M\dot{\hat{X}}^v + C\hat{X}^v + K\hat{X}^d = F \end{cases} \tag{16}$$

Note that we no longer have "$\dot{\hat{X}}^d = \hat{X}^v$", which is why we have introduced the new notation $(\hat{X}^d\ \hat{X}^v)^T$, instead of $(\hat{Y}\ \dot{\hat{Y}})^T$. Then the dynamics of the error $\tilde{X} = (\tilde{X}^d\ \tilde{X}^v)^T = (Y - \hat{X}^d\ \dot{Y} - \hat{X}^v)^T$ gives

$$\begin{cases} K\dot{\tilde{X}}^d = K\tilde{X}^v - \gamma(H^d)'H^d\tilde{X}^d - \gamma(H^d)'(\epsilon_h + \chi) \\ M\dot{\tilde{X}}^v + C\tilde{X}^v + K\tilde{X}^d = 0 \end{cases} \tag{17}$$

Introducing the classical energy norm for mechanical systems, namely, the sum of kinetic energy and strain energy

$$\|X\|_{\mathcal{E}}^2 = \frac{1}{2}(X^v)^T M X^v + \frac{1}{2}(X^d)^T K (X^d) = X^T N X,$$

for

$$X = \begin{pmatrix} X^d \\ X^v \end{pmatrix} \text{ and } N = \frac{1}{2}\begin{pmatrix} K & 0 \\ 0 & M \end{pmatrix},$$

then multiplying the first equation in (16) by $(\tilde{X}^d)^T$ and the second one by $(\tilde{X}^v)^T$ we have

$$\begin{aligned} \frac{d}{dt}\tilde{X}^T N \tilde{X} &= \frac{d}{dt}\left(\tfrac{1}{2}(\tilde{X}^v)^T M\tilde{X}^v + \tfrac{1}{2}(\tilde{X}^d)^T K\tilde{X}^d\right) \\ &= -\gamma(\tilde{X}^d)^T(H^d)'H^d\tilde{X}^d - (\tilde{X}^v)^T C\tilde{X}^v - \gamma(\tilde{X}^d)^T(H^d)'(\epsilon_h + \chi), \end{aligned} \tag{18}$$

hence the choice (15) introduces a new dissipative term involving the displacement error $\tilde{X}^d$.

Note that – in addition to the gain parameter γ – the filter design depends on the choice of the space in which the adjoint operator $(H^d)'$ is considered. Namely, for instance considering an observation space with a norm of L^2 type introduces a mass operator (or matrix in the finite element computations), similar to what is used in collocated stabilization [19]. Denoting this norm matrix in the observation space by W^{-1}, the adjoint $(H^d)'$ can be identified with $(H^d)^T W^{-1}$ for this norm. However, in collocated DVF strategies the dissipative term involves the velocity– instead of the displacement here – hence is amplified compared to the present case by a factor of the order of ω^2 for an eigenmode of associated eigenfrequency ω. In order to have a comparable high frequency effect here, we may want to use a stiffness operator – namely, corresponding to an H^1 space – for the adjoint operation instead of a mass operator. Of course, we cannot apply the real stiffness operator since the observation is only partial. Nevertheless, we can use the stiffness operator on a complete displacement field reconstructed by applying a lifting procedure on the partial measurement. Note that this is of course different from estimation by interpolation, which would merely use this lifted value as an estimation. Here instead, we use this interpolation as one step in a procedure that can also be interpreted as a preconditioning technique in the filter.

From a practical point of view, the lifting can be effectively performed using a Schur complement method inspired from domain decomposition methods (see e.g. [24]), which amounts to solving

$$\begin{pmatrix} 0 & H^d \\ (H^d)^T & K \end{pmatrix}\begin{pmatrix} \Lambda_Z \\ X_Z \end{pmatrix} = \begin{pmatrix} Z \\ 0 \end{pmatrix}, \tag{19}$$

for any Z in the image space of H^d. This means that X_Z is the solution of the constrained minimization problem

$$\min_{X \text{ s.t.} H^d X = Z} \tfrac{1}{2} X^T K X, \tag{20}$$

and Λ_Z represents the Lagrange multiplier associated with the constraint "$H^d X = Z$". Provided this system is solvable in Λ_Z – see below for circumventing this condition – we can uniquely define the linear operator S such that $\Lambda_Z = -SZ$. The filter is then given by

$$(H^d)' Z = K X_Z = (H^d)^T S Z,$$

hence the filter equation becomes

$$\begin{cases} K\dot{\hat{X}}^d = K\hat{X}^v + \gamma (H^d)^T S (Z - H^d \hat{X}^d) \\ M\dot{\hat{X}}^v + C\hat{X}^v + K\hat{X}^d = F \end{cases} \tag{21}$$

leading to

$$\frac{d}{dt} \tilde{X}^T N \tilde{X} = -\gamma (\tilde{X}^d)^T (H^d)^T S H^d \tilde{X}^d - (\tilde{X}^v)^T C \tilde{X}^v - \gamma (\tilde{X}^d)^T (H^d)' (\epsilon_h + \chi). \tag{22}$$

The filter is no longer collocated, but in essence the operator $(H^d)^T S H^d$ appearing in the error equation is then designed to behave like K. In fact, denoting by X_{corr} the lifting of $Z - H^d \hat{X}^d$ by the Schur complement procedure we can see that the first equation of the estimation system can be rewritten as

$$\dot{\hat{X}}^d = \hat{X}^v + \gamma X_{corr}. \tag{23}$$

Incidentally, if we were to observe the complete displacement – namely, the ideal case with $H^d = Id$, $X_Z = Z$ – we would have exactly $K = (H^d)' H^d$. We henceforth refer to this filter as the "Schur Displacement Feedback" (SDF), whereas we will call the L^2 filter the "Direct Displacement Feedback" (DDF).

Note that we can approximate the solution of the above constrained minimization problem by instead solving the penalized problem

$$\min_X \tfrac{1}{2} \big\{ X^T K X + \kappa \| Z - H^d X \|^2_{W^{-1}} \big\}, \tag{24}$$

which leads to the modified algebraic system

$$\begin{pmatrix} -\frac{1}{\kappa} W & H^d \\ (H^d)^T & K \end{pmatrix} \begin{pmatrix} \Lambda_Z \\ X_Z \end{pmatrix} = \begin{pmatrix} Z \\ 0 \end{pmatrix}, \tag{25}$$

where κ denotes a "large" penalization parameter. When κ tends to infinity the solution of this problem tends to the state that minimizes (20) with Z_{proj} – the projection of Z on the image space of H^d – substituted for Z in the constraint. Therefore, this penalized procedure provides a meaningful result even when H^d is not surjective, in which case the exact constraint "$H^d X = Z$" is not always solvable. This strategy can also be interpreted as a Tikhonov regularization by the elastic deformation energy, $1/\kappa$ playing then the role of the regularization parameter. Another key advantage of this penalized version is that the Lagrange multiplier can be eliminated in the resulting equations, hence we can obtain the following explicit expression of the filter

$$(H^d)^T S = \kappa K \big(K + \kappa (H^d)^T W^{-1} H^d \big)^{-1} (H^d)^T W^{-1}, \tag{26}$$

which leads to the estimator equations

$$\begin{cases} K\dot{\hat{X}}^d = K\hat{X}^v + \gamma\kappa K\big(K + \kappa(H^d)^T W^{-1} H^d\big)^{-1}(H^d)^T W^{-1}(Z - H^d\hat{X}^d) \\ M\dot{\hat{X}}^v + C\hat{X}^v + K\hat{X}^d = F \end{cases} \tag{27}$$

Of course, in practice we can eliminate the matrix K in the first equation, but we retain it in this expression to preserve the formal similarity with the DDF equations. We also point out that the filtering term in this system is formally similar to the Kalman classical expression, with the stiffness matrix substituted for the so-called "a priori covariance matrix". In the sequel we will use this penalized form of the SDF estimator, both in order to take advantage of this explicit filter equation without any Lagrange multiplier, and to avoid solvability issues. Furthermore, the expression (27) shows that the SDF estimator can be computed in practice with no additional complexity with respect to the DDF.

Remark: Assuming that the semi-group generated by the dynamical system (17) associated with the estimation error is exponentially stable with a time constant τ, the error analysis of [14] can be reproduced here in an identical manner. We then infer an *a priori* error estimate of the form

$$\|\tilde{X}\|_N \leq C\big(e^{-T/\tau}\|\zeta_X\|_N + \gamma\sqrt{\tau}\|\epsilon_h + \chi\|_{L^2([0,T],\mathcal{O})}\big), \tag{28}$$

where the symbol $\mathcal{O}$ denotes a suitable norm in the observation space. Note that this estimate only contains source terms that represent *actual uncertainties* in the observed system. This error estimate also shows how the estimation error may be influenced by the discretization considered, namely, through ϵ_h. In some specific cases of collocated feedback the exponential stability can be mathematically established – which crucially conditions the above error estimate – but in the present case the feedback control cannot be applied on a real system, hence we do not know of existing results in the control litterature. Nevertheless, we can also obtain numerical estimates of the time constants by computing the poles of the numerical estimation system considered, as illustrated in the next section.

3.2 Analysis of the state estimator

In order to assess the state estimator we compute the poles of the associated time-continuous eigenproblem

$$\begin{pmatrix} \gamma(H^d)'H^d & K \\ -K & -C \end{pmatrix} V = \lambda \begin{pmatrix} K & 0 \\ 0 & M \end{pmatrix} V. \tag{29}$$

We compare in Figure 4 the poles of the original system and the poles obtained with the DDF, SDF, and SDF with full displacement measurements. We note that the DDF primarily damps the low frequencies whereas the SDF behaves like the ideal complete measurement case for a large frequency band.

Regarding the SDF, we recall that in the ideal complete measurement case, the damping of the poles is improved when increasing the gain parameter γ until the fundamental mode reaches the real axis, see Figure 5 [19]. This corresponds to the optimal gain, since when further increasing this parameter the two previously-conjugate poles remain on the real axis, and one of them progresses towards the origin, namely, with decreasing damping. In fact, in the ideal case of complete observation $(H^d)'H^d = K$ in the above system and the poles are solutions of the quadratic eigenvalue problem (QEP), see [23],

$$\lambda^2 MV + \lambda(\gamma M + \eta K)V + (\gamma\eta + 1)KV = 0, \tag{30}$$

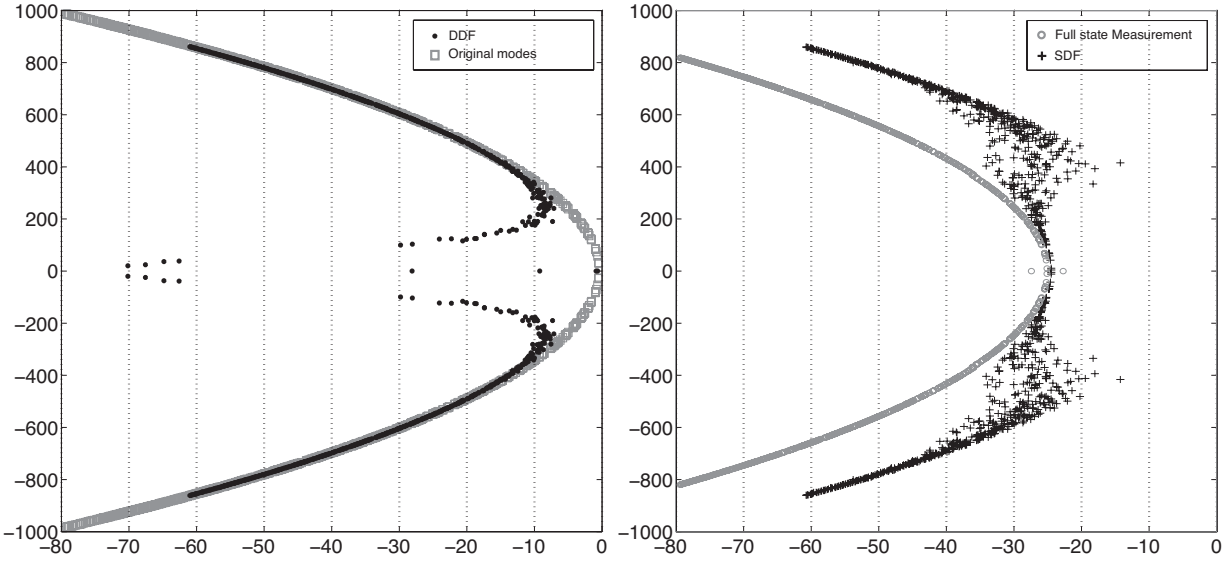

Figure 4: Poles of the DDF (left) and SDF (right) estimators with cell measurements

hence these poles directly relate to the poles of the system with proportional damping $C = \alpha M + \beta K$ corresponding to the classical QEP

$$\tilde{\lambda}^2 MV + \tilde{\lambda}(\alpha M + \beta K)V + KV = 0, \tag{31}$$

with $\tilde{\lambda} = \frac{\lambda}{\sqrt{\gamma\eta+1}}$, $\alpha = \frac{\gamma}{\sqrt{\gamma\eta+1}}$, $\beta = \frac{\eta}{\sqrt{\gamma\eta+1}}$. Then the computation can be performed analytically, and we find for the optimal gain value the following first order expression:

$$\gamma_{\text{opt}} = \sqrt{2}\,\omega_0 + \text{h.o.t}, \tag{32}$$

with higher order terms in $O(\omega_0\eta)^2$, where ω_0 denotes the fundamental frequency of the system (in our case $\omega_0\eta \sim 10^{-2}$). Note that this gives a good estimate of the optimal gain – valid for any discretization – as soon as an adequate value of the "exact" fundamental frequency is known, and we also used this gain value in the case of partial measurements in our numerical simulations.

In fact, with the gain value chosen for the DDF to effectively damp a sufficient number of modes, we have one low energy real pole near the imaginary axis, while all the poles of the SDF have a real value below $-14\,\text{s}^{-1}$. This has an impact in the estimation errors, particularly for initial conditions that have a wide modal content. In Figure 6 we display the energies of the SDF and the DDF homogeneous estimation errors – namely with zero ϵ_h and χ in (17) – when using the time discretization scheme described in the next section, and for two different initial conditions:

Pressure I.C.: A static displacement obtained by imposing a pressure of 10^3Pa on the endocardium, the order of magnitude of the ventricular filling pressure. This initial condition corresponds to an error in energy of about 1% of the maximum energy in the system during the period considered and to a volume increase of about 30%.

Modal I.C.: A static displacement provided by a linear combination of the first ten modes of the undamped system with equal coefficients. We deliberately used a higher energy initial – namely 10% of the maximum energy – condition in this case to assess the efficiency of the filters in more difficult conditions.

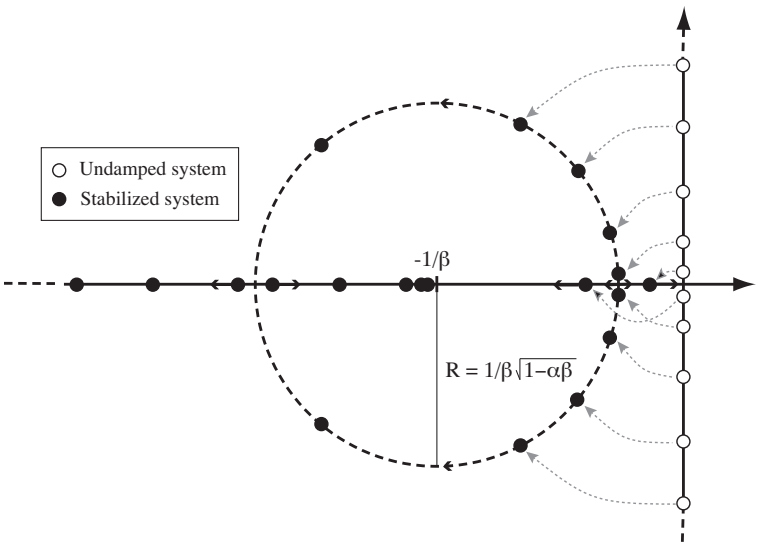

Figure 5: Pole locus for proportional damping

We can see a slight improvement when using the SDF with pressure initial condition, but more importantly, the SDF is much more robust with respect to changes in the initial condition whereas the DDF behavior is hindered by the low damped mode which is excited by the modal initial condition.

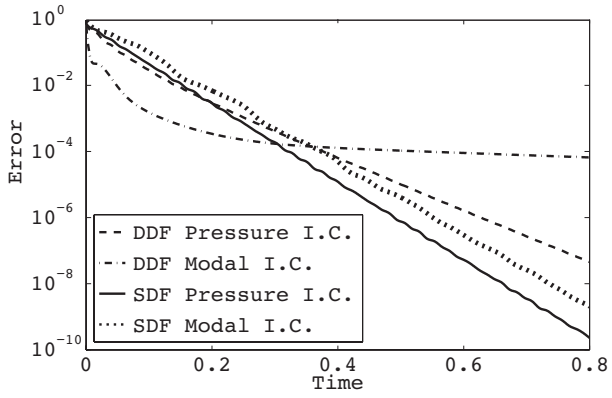

Figure 6: Homogeneous SDF and DDF error energies (scaled by initial error)

In order to demonstrate the performance of the DDF and SDF filters, we now consider the estimation when including the measurement and discretization errors for the pressure initial condition. We have used the two types of measurement errors described above in our simulations, without any noticeable difference in the results. In Figure 7 we show the estimated volumes compared to the reference, and to the volume computed without incorporating the filtering term, which illustrates the effective trajectory tracking for this meaningful physiological indicator.

We investigate the error in more details in Figure 8 by plotting the estimation errors compared to the errors associated with

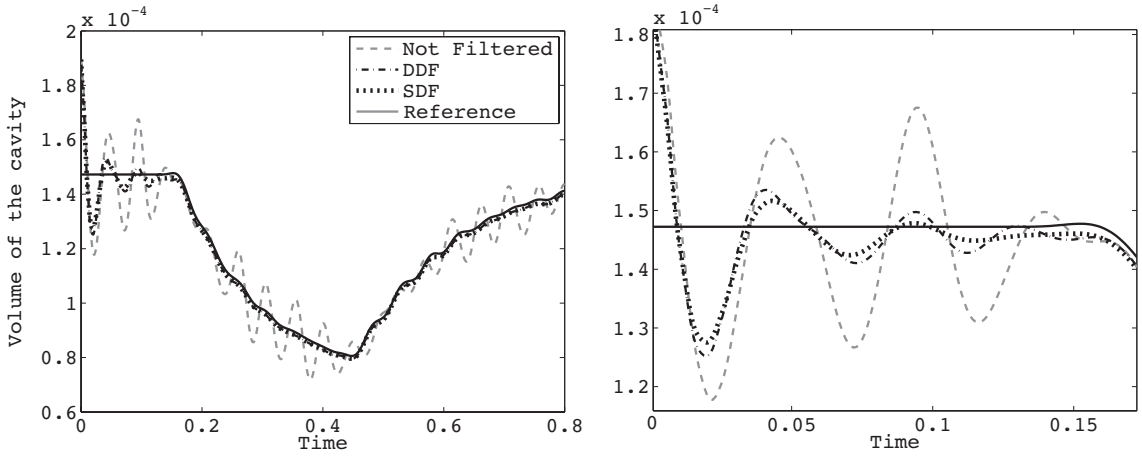

Figure 7: Volume with and without filters (left) and zoom near $t = 0$ (right)

- the solution of the direct problem (5) generated with the desired mesh without initial condition error (this gives the curve labeled "discretization error" in the figure);
- the reference solution interpolated in the desired mesh at each time step (the "interpolation error").

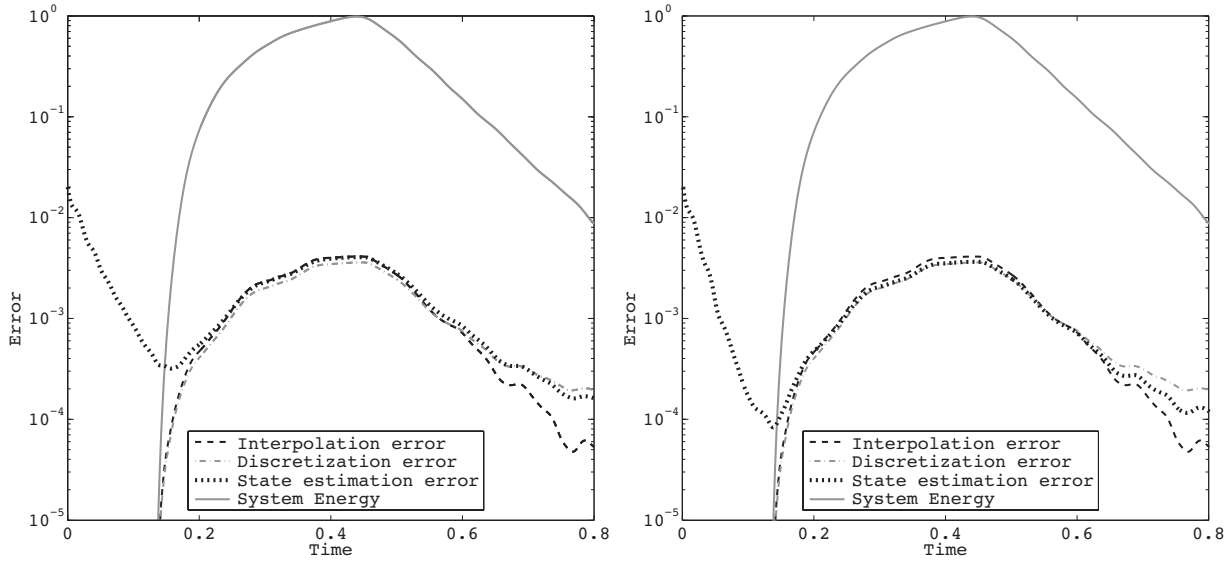

Figure 8: Comparison of estimation, interpolation and discretization errors: DDF (left) and SDF (right)

Both strategies are very effective in this case – and better indeed than the discretization error after the activation has started – but the SDF estimation is still more accurate, as seen in particular in the beginning of the estimation window. Note that – of course – the estimation error is always bounded from below by the interpolation error.

3.3 Time discretisation

As mentioned above, we use a Newmark scheme to perform the time discretization of the system. In the context of small displacements, hence of linear mechanical systems, it is well known that this scheme does not introduce numerical dissipation or spurious energy sources. Namely, let us introduce the time discretized variable $X_n = (Y_n \ \dot{Y}_n)^T$ which represents the approximation of $X(n\Delta t)$. The Newmark scheme consists – in fact – in solving the system at time $t = (n + \frac{1}{2})\Delta t$ using the standard trapezoidal rules leading to

$$\begin{cases} \dfrac{Y_{n+1} - Y_n}{\Delta t} = \dfrac{\dot{Y}_{n+1} + \dot{Y}_n}{2} \\ M\dfrac{\dot{Y}_{n+1} - \dot{Y}_n}{\Delta t} + C\dfrac{\dot{Y}_{n+1} + \dot{Y}_n}{2} + K\dfrac{Y_{n+1} + Y_n}{2} = F_{n+\frac{1}{2}} \\ Y_{n=0} = Y_0 + \zeta^d, \quad \dot{Y}_{n=0} = \dot{Y}_0 + \zeta^v \end{cases} \tag{33}$$

Using classical identities, in the absence of external loading the discrete energy then iteratively decreases as

$$X_{n+1}^T N X_{n+1} - X_n^T N X_n = -\dot{Y}_{n+\frac{1}{2}} C \dot{Y}_{n+\frac{1}{2}}.$$

In the context of our estimator we cannot use the variables $(Y_n \ \dot{Y}_n)$ since the velocity variable differs from the derivative of the displacement variable. We then introduce $\hat{X}_n = \hat{X}(n\Delta t) = (\hat{X}_n^d \ \hat{X}_n^v)^T$. A similar trapezoidal scheme then gives

$$\begin{cases} K\dfrac{\hat{X}_{n+1}^d - \hat{X}_n^d}{\Delta t} = K\dfrac{\hat{X}_{n+1}^v + \hat{X}_n^v}{2} + \gamma (H^d)' \left(Z_{n+\frac{1}{2}} - H^d \dfrac{\hat{X}_{n+1}^d + \hat{X}_n^d}{2} \right) \\ M\dfrac{\hat{X}_{n+1}^v - \hat{X}_n^v}{\Delta t} + C\dfrac{\hat{X}_{n+1}^v + \hat{X}_n^v}{2} + K\dfrac{\hat{X}_{n+1}^d + \hat{X}_n^d}{2} = F_{n+\frac{1}{2}} \\ \hat{X}_{n=0}^d = Y_0, \quad \hat{X}_{n=0}^v = \dot{Y}_0 \end{cases} \tag{34}$$

which leads with the same identities to the following discrete energy evolution

$$\tilde{X}_{n+1}^T N \tilde{X}_{n+1} - X_n^T N X_n = -\gamma (\tilde{X}_{n+\frac{1}{2}}^d)^T (H^d)' H^d \tilde{X}_{n+\frac{1}{2}}^d + (\tilde{X}_{n+\frac{1}{2}}^v)^T C \tilde{X}_{n+\frac{1}{2}}^v - \gamma (\tilde{X}_{n+\frac{1}{2}}^d)^T (H^d)' (\chi + \epsilon_h)_{n+\frac{1}{2}}. \tag{35}$$

We point out that this scheme is implicit in both equations with non diagonal operators – unlike in the first equation of (33). In practice this leads to the inversion of a $2N$ degrees of freedom linear system.

Alternatively, in the case of the SDF filter which we now focus on, we can choose to solve the estimator dynamics with an iterative method, provided we can find a good – and easily invertible – preconditionner. In this context, we point out that our estimator would be

$$\begin{cases} K\dfrac{\hat{X}_{n+1}^d - \hat{X}_n^d}{\Delta t} = K\dfrac{\hat{X}_{n+1}^v + \hat{X}_n^v}{2} - \gamma K\dfrac{\hat{X}_{n+1}^d + \hat{X}_n^d}{2} + R_{n+\frac{1}{2}} \\ M\dfrac{\hat{X}_{n+1}^v - \hat{X}_n^v}{\Delta t} + C\dfrac{\hat{X}_{n+1}^v + \hat{X}_n^v}{2} + K\dfrac{\hat{X}_{n+1}^d + \hat{X}_n^d}{2} = F_{n+\frac{1}{2}} \end{cases} \tag{36}$$

if the whole state were available in the measurement, recall Section 3.1. In fact, we can prove that this system can be a good preconditionner of our SDF estimator for any observation operator. Indeed, the SDF leads to a linear system of the form

$$\begin{pmatrix} K + \frac{\gamma \Delta t}{2} (H^d)^T S H^d & -\frac{\Delta t}{2} K \\ \frac{K}{2} & \frac{M}{\Delta t} + \frac{C}{2} \end{pmatrix} \begin{pmatrix} \hat{X}_{n+1}^d \\ \hat{X}_{n+1}^v \end{pmatrix} = \text{RHS},$$

which gives, when eliminating $\hat{X}^v_{n+1}$ using the second equation,

$$K_{\rm SDF}\hat{X}^d_{n+1} = \text{RHS}, \quad \text{with } K_{\rm SDF} = K + \frac{\gamma\Delta t}{2}(H^d)^T S H^d + \frac{\Delta t}{4} K\left(\frac{M}{\Delta t} + \frac{C}{2}\right)^{-1} K. \tag{37}$$

The preconditionner is obtained by simply substituting K for $(H^d)^T S H^d = (H^d)' H^d$, hence the governing equation is instead

$$K_{\rm pre}\hat{X}^d_{n+1} = \text{RHS}, \quad \text{with } K_{\rm pre} = K + \frac{\gamma\Delta t}{2}K + \frac{\Delta t}{4} K\left(\frac{M}{\Delta t} + \frac{C}{2}\right)^{-1} K.$$

From (26) we infer the identity

$$(H^d)^T S H^d + K\big(K + \kappa (H^d)^T W^{-1} H^d\big)^{-1} K = K,$$

hence, we have

$$0 \le (H^d)^T S H^d \le K,$$

in the usual sense of positive symmetric matrix inequalities, and this directly implies

$$K_{\rm SDF} \le K_{\rm pre}.$$

In addition,

$$\frac{K_{\rm pre}}{1 + \frac{\gamma\Delta t}{2}} = K + \frac{\frac{\Delta t}{4}}{1 + \frac{\gamma\Delta t}{2}} K\left(\frac{M}{\Delta t} + \frac{C}{2}\right)^{-1} K \le K_{\rm SDF}.$$

Therefore,

$$K_{\rm SDF} \le K_{\rm pre} \le \big(1 + \frac{\gamma\Delta t}{2}\big) K_{\rm SDF},$$

which shows that the conditionning of the preconditionned system is close to 1 when $\frac{\gamma\Delta t}{2}$ is small.

From an algorithmic point of view, note that one iterative step only requires the inversion of two systems of N degrees of freedom each. Namely, to compute the action of the real system (discretized from (27)) we first need to invert $K + \kappa (H^d)^T W^{-1} H^d$. Then, in the actual preconditionner we do not have K in the first line since it can be eliminated from the first line of the real system as well, hence this first preconditionner equation gives a straightforward expression of $\hat{X}^v_{n+1}$ with respect to $\hat{X}^d_{n+1}$. When substituting in the second preconditionner equation we thus obtain an equation in the single unknown $\hat{X}^d_{n+1}$ with the matrix $(\frac{M}{\Delta t} + \frac{C}{2})(\frac{2}{\Delta t} + \gamma) + \frac{K}{2}$ to be inverted.

In practice, using a GMRES algorithm we obtained the solution with a maximum of four iterations at each time step for an accuracy compatible with the orders of magnitude of estimation errors, as can be checked in Figure 9 where we plot the difference between the estimation errors obtained with a direct solver and with the above iterative procedure (to be compared with the errors shown in Figure 8).

3.4 Boundary displacement measurements

In some other imaging modalities displacements are obtained with enhanced accuracy along the boundaries. For instance, optical flow or registration methods (see [1, 17, 15]) that establish similarities between snapshots are more reliable – in general – in strong gradient regions of the image associated with contours.

As a consequence, we assume here that the measurements are displacements (or normal displacements in a second part) on a subpart Γ_m of the boundary domain $\partial\Omega$. Namely, $\mathcal{H}x = (\mathcal{H}^d\ 0)(\underline{y}\ \underline{\dot{y}})^T$

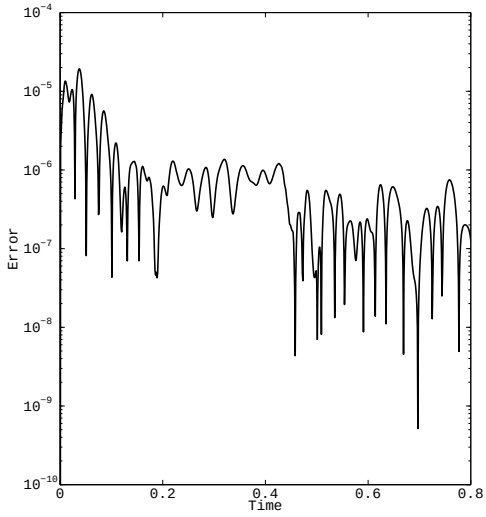

Figure 9: Difference between estimation errors for direct and iterative SDF solutions

consists of the trace of the displacement field on Γ_m – well-defined since $\underline{y} \in H^1(\Omega)$. We also define by H the discrete observation operator, namely, the operator giving the trace on Γ_m of the displacement part of a discrete state vector. Since H only acts on displacements – like the continuous observation operator $\mathcal{H}$ – we will also use the expression

$$H = (H^d\ 0) = (\Im_\Gamma T_\Gamma\ 0),$$

where T_Γ is defined as a matrix that selects the degrees of freedom located on Γ_m, and $\Im_\Gamma$ as the operator that interpolates a surface field from these degrees of freedom. Note that – clearly – here the discrete observation operator H^d is not surjective in the whole space of traces, hence the penalized version of the SDF filter is particularly valuable in such a case.

First, we show in Figure 10 the resulting poles for the DDF and SDF filters in the case of measurements available only at the endocardium with results similar to those with cell measurements, although the SDF pole locus is not quite as close to the ideal measurement curve. This could be expected as we only have very partial measurements, namely, on one outer surface only, used for the Schur complement lifting. By contrast, we also show in the figure the SDF poles obtained with measurements on the complete boundary, and these poles are much closer to the ideal locus, indeed.

3.5 Case of normal displacement measurements on the boundary

In fact, material points can hardly be distinguished on a contour – except for particular landmarks – hence only surface displacements can be well captured. Namely, the above mentioned image processing techniques recover with better accuracy the displacements normal to the boundaries $\underline{y} \cdot \underline{\nu}$ rather than the full displacement vectors. In this case $\mathcal{H}^d$ simply gives the normal component of the trace as for its discrete counterpart H^d. Then, the DDF operator $(H^d)'H^d$ – associated with the $L^2(\Gamma_m)$ norm – has the variational form

$$\int_{\Gamma_m} (\underline{\tilde{y}} \cdot \underline{\nu})(\underline{\nu} \cdot \underline{\delta y})\, dS. \tag{38}$$

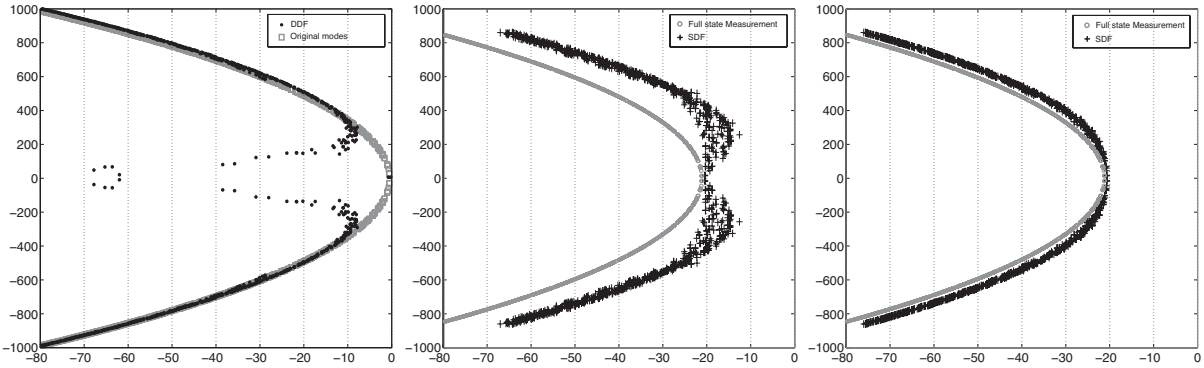

Figure 10: DDF and SDF poles for endocardium measurements (left and center), SDF for the whole boundary measurements (right)

The resulting poles are shown Figure 11 for the DDF and SDF poles with measurements of the normal displacements on the whole boundary. We can see that the damping is less effective as with measurements of the complete displacement vectors. This can be interpreted as related to a lack of observability in the system. This is confirmed by checking that a similar locus is obtained when measuring any scalar component of the displacement vector instead of the normal value, although the low damping modes differ in each case.

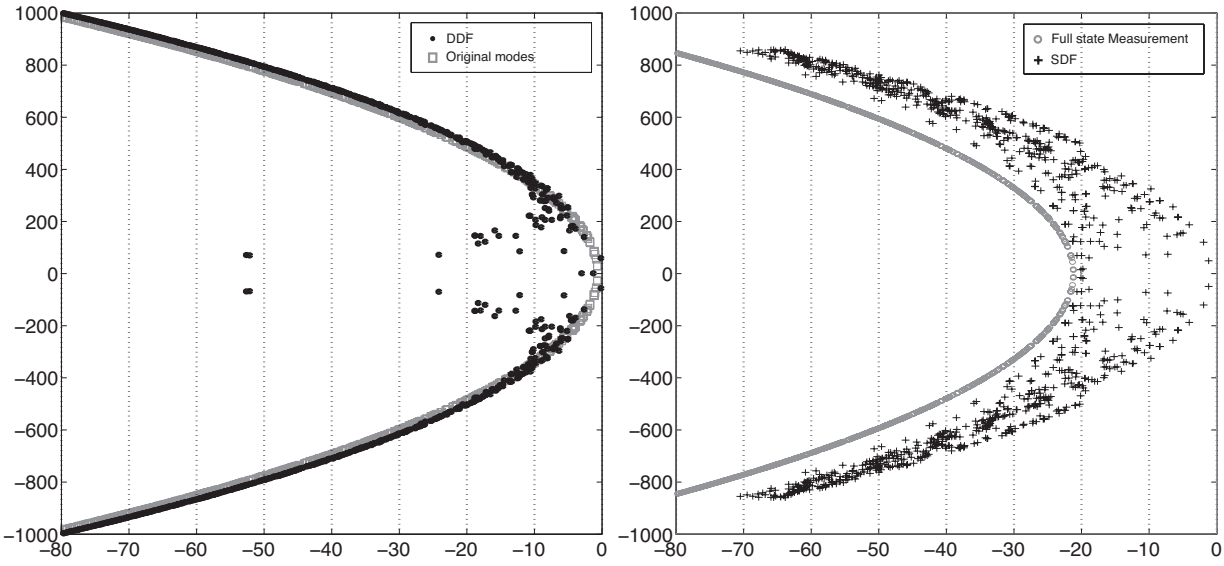

Figure 11: Poles of the DDF (left) and SDF (right) estimators with boundary normal displacements

4 Estimation from Eulerian position measurements

4.1 Estimator in continuous time

In this section we are interested in the situation where we only know the position of the body at different time steps in a Eulerian framework. Namely, the spatial description consists in segmented

images (typically along the heart beat), which we consider in the form of meshed surfaces – classically obtained using marching cubes and automatic mesh generation algorithms, for example. As regards time sampling, we only have $N_{\Delta T}$ available snapshots of the configuration at successive time steps $k\Delta T,\ 1 \leq k \leq N_{\Delta T}$ – different from (and in general much coarser than) the computational time steps. We thus define as (S_k) the series of surfaces corresponding to the segmented snapshots. These measurements cannot be easily expressed from the state x with an operator $\mathcal{H}$ (even for a nonlinear operator) in the form

$$Z = \mathcal{H}(x) + \chi.$$

Nevertheless, in order to determine if the state matches a given snapshot, a natural idea is to compute the distance between the boundary of the estimator and the surface representing the snapshot. For example, at time $t = k\Delta t$ the estimator matches the surface S_k when

$$\operatorname{dist}(\underline{\mathrm{x}}_t, S_k) = 0, \quad \forall \underline{\mathrm{x}}_t \in \partial\hat{\Omega}_t, \tag{39}$$

for the spatial position $\underline{\mathrm{x}}_t$ corresponding to the deformed configuration of the estimator $\hat{\Omega}_t$. This can be compared with the usual measurement matching condition

$$Z - H(\hat{X}) = 0, \tag{40}$$

hence, the distance operator represents an extension of the usual observation quantity $Z - H(\hat{X})$. Note that we only need this quantity in the filter, since we compare the observation created by the estimator with the real measurement, recall (11). Therefore, we propose to directly use the computation of the distance at each point of the boundary domain to feed the filter.

Since we are in a Lagrangian formulation we write the current configuration $\underline{\mathrm{x}}_t$ as the sum $\underline{\mathrm{x}}_t = \underline{\mathrm{x}} + \underline{y}$ with $\underline{y} = \underline{y}(\underline{\mathrm{x}})$ the displacement field, and by extension we denote the complete operator on the finite element model by $\operatorname{dist}(\hat{X}^d, S_k)$. Here we directly take into account the time sampling of the data – namely, the segmented images – hence we construct the operator at all times by interpolation. We then define

$$W_d(\hat{X}^d, t) = \alpha_k(t) \operatorname{dist}(\hat{X}^d, S_k) + (1 - \alpha_k(t)) \operatorname{dist}(\hat{X}^d, S_{k+1}), \quad \forall t \in [k\Delta T, (k+1)\Delta T]. \tag{41}$$

We point out that the distance is signed, namely, for any point $\underline{\mathrm{x}}$ the distance to a boundary $S = \partial D$ of a closed domain D is such that the sign of $\operatorname{dist}(\underline{\mathrm{x}}, S) < 0$ if $\underline{\mathrm{x}}$ is inside D and $\operatorname{dist}(\underline{\mathrm{x}}, S) > 0$ if $\underline{\mathrm{x}}$ is outside D. Therefore this interpolation is meaningful even if the point considered is between two surfaces S_k and S_{k+1}, see Figure 12. Note that this is consistent with our extension of the observation quantity $Z - H(\hat{X})$ since the interpolation of Section 3.1 can be rephrased as

$$(\alpha_k(t)Z_k + (1 - \alpha_k(t))Z_{k+1}) - H(\hat{X}) = \alpha_k(t)(Z_k - H(\hat{X})) + (1 - \alpha_k(t))(Z_{k+1} - H(\hat{X})).$$

The operator W_d is nonlinear in X^d, so we cannot use it directly in a filter formulation before finding an equivalent to H'_d. Note that the derivative of the least square term $\frac{1}{2}\|Z - H(X)\|^2$ gives the expression $-\frac{\partial H}{\partial X}'(Z - H(X))$ which is classically employed in nonlinear filtering. In our case, we thus use $\frac{\partial W_d}{\partial Y}'W_d$ corresponding to the minimization criterion $\frac{1}{2}W_d^2$. In order to compute $\frac{\partial W_d}{\partial Y}$, we differentiate the distance using the notations of Figure 12

$$\begin{aligned}
\frac{\partial \operatorname{dist}(\underline{\mathrm{x}} + \underline{y}, S_k)}{\partial \underline{y}} \cdot \underline{dy} &= -\frac{\partial((\underline{MP}) \cdot \underline{\nu}_{S_k})}{\partial \underline{y}} \cdot \underline{dy} \\
&= \left(\frac{\partial \underline{M}}{\partial \underline{y}} \cdot \underline{dy}\right) \cdot \underline{\nu}_{S_k} - \left(\frac{\partial \underline{P}}{\partial \underline{y}} \cdot \underline{dy}\right) \cdot \underline{\nu}_{S_k} - \underline{MP} \cdot \left(\frac{\partial \underline{\nu}_{S_k}}{\partial \underline{y}} \cdot \underline{dy}\right) \\
&= \left(\frac{\partial \underline{M}}{\partial \underline{y}} \cdot \underline{dy}\right) \cdot \underline{\nu}_{S_k}.
\end{aligned}$$

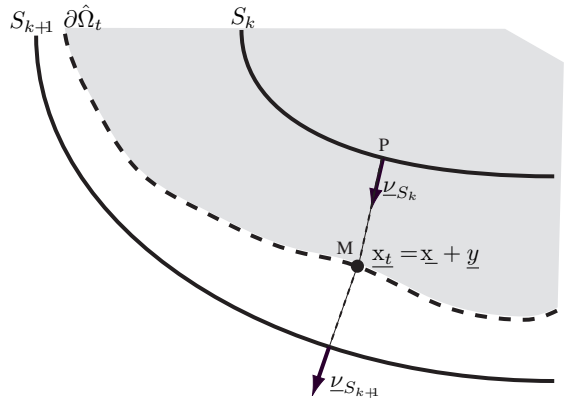

Figure 12: Projection of simulated contour on segmented image surfaces

In other words,

$$\nabla_y(\mathrm{dist}(\underline{x}+\underline{y}, S_k)) = \underline{\nu}_{S_k}. \tag{42}$$

Hence, our filter $\left(\frac{\partial W_d}{\partial Y}\right)' W_d(Y,t)$ has the associated variational term

$$\int_{\Gamma_m} \mathrm{dist}(\underline{x}+\underline{y})(\underline{\nu}_{S_k} \cdot \underline{\delta y})\, dS, \tag{43}$$

when considering the adjoint for the $L^2(\Gamma_m)$-norm. The state estimator system is then

$$\begin{cases} K\dot{\hat{X}}^d = K\hat{X}^v - \gamma\left(\dfrac{\partial W_d}{\partial Y}\right)' W_d(\hat{X}^d, t) \\ M\dot{\hat{X}}^v + C\hat{X}^v + K\hat{X}^d = F \end{cases} \tag{44}$$

With the expression in (43) for the L^2-norm, we note that this approach bears some resemblance with image force methods used in image processing, see e.g. [7], and [21] for using image forces with dynamical deformable models. Here, however, we include this term as a correction in the first equation of the dynamics and not as a force. In addition, when using the SDF form the correction term is no longer collocated as in (43). Recalling (23) in this case the first equation of the estimator system instead amounts to

$$\dot{\hat{X}}^d = \hat{X}^v + \gamma X_{corr},$$

with X_{corr} defined as the displacement vector obtained by lifting normal boundary displacements equal to the opposite of the (signed) distance to the image surface. Note that this correction is performed throughout the volume, whereas the DDF correction only acts on the boundary.

We point out that the error system is no longer autonomous but when linearizing around the actual trajectory which satisfies $W_d(X^d, t) = 0$, we obtain

$$\begin{cases} K\dot{\tilde{X}}^d = K\tilde{X}^v - \gamma\left(\dfrac{\partial W_d}{\partial Y}(X^d,t)\right)'\left(\dfrac{\partial W_d}{\partial Y}(X^d,t)\right)\tilde{X}^d \\ M\dot{\tilde{X}}^v + C\tilde{X}^v + K\tilde{X}^d = 0 \end{cases} \tag{45}$$

Hence, the linearized estimation error is exactly dissipative like in (35) with $\frac{\partial W_d}{\partial Y}(X^d,t)$ substituted for H, leading – with the $L^2(\Gamma_m)$-norm adjoint – to the variational term

$$\int_{\Gamma_m} (\underline{\tilde{y}} \cdot \underline{\nu}_{S_k})(\underline{\nu}_{S_k} \cdot \underline{\delta y})\, dS,$$

This term is similar to (38) but here the normal vectors $\underline{\nu}_{S_k}$ vary due to the motion of S_k, the boundary of the actual system.

In practice, we extract the surface of the reference simulation at each time step $k\Delta T$, $1 \leq k \leq N_{\Delta T}$, and we compute a signed distance between the estimated surface and the corresponding reference surfaces using the algorithm presented in [3]. This procedure allows to effectively compute the signed distance for any point $\underline{x}$ to a boundary mesh.

4.2 Time discretization

Following the same time discretization as in Section 3.3, we will discretize the observation term with the midpoint filtering quantity

$$\left(\frac{\partial W_d}{\partial Y}\Big(\frac{\hat{X}^d_{n+1}+\hat{X}^d_n}{2}, \frac{t_{n+1}+t_n}{2}\Big)\right)' W_d\Big(\frac{\hat{X}^d_{n+1}+\hat{X}^d_n}{2}, \frac{t_{n+1}+t_n}{2}\Big).$$

Therefore, the discrete energy of the linearized error decreases following the same identity as (35) with $(\frac{\partial W_d}{\partial Y}(\hat{X}^d_{n+\frac{1}{2}}, t_{n+\frac{1}{2}}))'(\frac{\partial W_d}{\partial Y}(\hat{X}^d_{n+\frac{1}{2}}, t_{n+\frac{1}{2}}))$ substituted for $(H_d)'H_d$. However, the nonlinearity of $W_d(X, Z)$ then imposes to resort to a Newton scheme even if the dynamical system itself is linear. In order to circumvent this difficulty we choose to linearize the above term with a second order extrapolated prediction to maintain the quadratic time consistency. We thus introduce

$$X_e = \frac{3X_n - X_{n-1}}{2},$$

such that $X_e - X_{n+\frac{1}{2}} = O(\Delta t^2)$ and replace

$$\boxed{\begin{aligned}&\left(\frac{\partial W_d}{\partial Y}(\hat{X}^d_{n+\frac{1}{2}}, t_{n+\frac{1}{2}})\right)' W_d(\hat{X}^d_{n+\frac{1}{2}}, t_{n+\frac{1}{2}}) \rightarrow \\ &\qquad\qquad \left(\frac{\partial W_d}{\partial Y}(\hat{X}^d_e, t_{n+\frac{1}{2}})\right)' \left(W_d(\hat{X}^d_e, t_{n+\frac{1}{2}}) + \Big(\frac{\partial W_d}{\partial Y}(\hat{X}^d_e, t_{n+\frac{1}{2}})\Big)(\hat{X}_{n+\frac{1}{2}} - \hat{X}_e)\right)\end{aligned}}$$

For the actual system we have

$$\begin{aligned} 0 &= W_d(Y_{n+\frac{1}{2}}, t_{n+\frac{1}{2}}) \\ &= W_d(Y_e, t_{n+\frac{1}{2}}) + \Big(\frac{\partial W_d}{\partial Y}(Y_e, t_{n+\frac{1}{2}})\Big)(Y_{n+\frac{1}{2}} - Y_e) \\ &\quad + \Big(\frac{\partial^2 W_d}{\partial Y^2}(Y_e, t_{n+\frac{1}{2}})\Big) : (Y_{n+\frac{1}{2}} - Y_e) \otimes (Y_{n+\frac{1}{2}} - Y_e) + o(\Delta t^4) \end{aligned} .$$

Therefore in the system of the linearized error the stabilization term becomes

$$\begin{aligned} -\gamma \left(\frac{\partial W_d}{\partial Y}(Y_e, t_{n+\frac{1}{2}})\right)' \Big(&\Big(\frac{\partial W_d}{\partial Y}(Y_e, t_{n+\frac{1}{2}})\Big)(\tilde{X}_{n+\frac{1}{2}}) \\ &+\Big(\frac{\partial^2 W_d}{\partial Y^2}(Y_e, t_{n+\frac{1}{2}})\Big) : \tilde{X}^d_e \otimes (Y_{n+\frac{1}{2}} - Y_e)\Big) + O(\Delta t^4) \end{aligned} \tag{46}$$

which is dissipative up to terms of order $O(\Delta t^2)$.

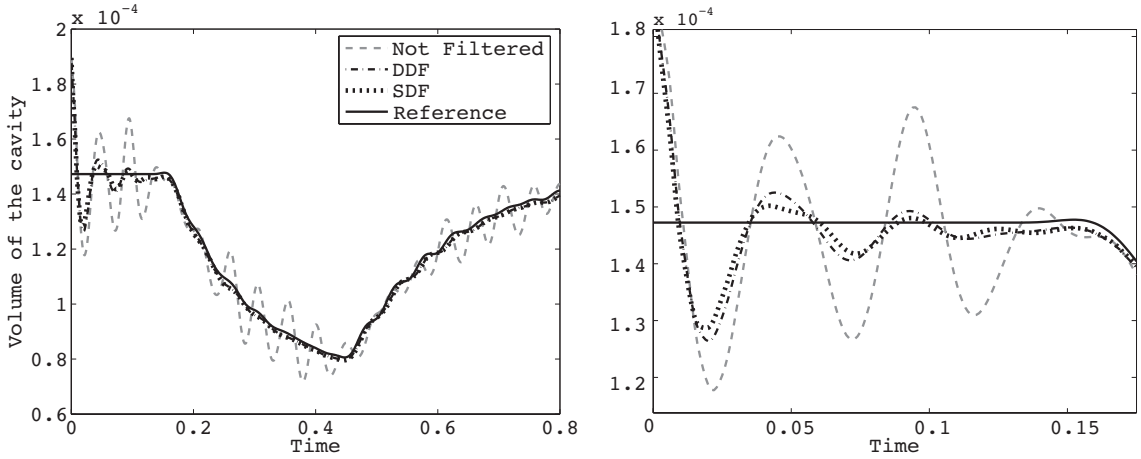

Figure 13: Estimated volume with and without filters (left) and zoom near $t = 0$ (right)

4.3 Estimation results

We display in Figure 13 the estimated volume obtained with the DDF and SDF filters for the pressure filling initial conditions. The estimation errors are shown in Fig. 14, also for the modal initial condition. In all cases, the whole boundary is considered using complete segmentations of the geometry. The performances of the filters are excellent in all cases, although the DDF is more sensitive to the modal initial condition as in the linear case. Here again, the effectiveness of the DDF in the pressure filling case was expected, since the gain was specifically tuned to damp the modes primarily excited by this loading. Note, however, that in the modal case only the SDF achieves a smaller estimation error than the discretization error. Hence, this shows that it is better to take advantage of the available measurements using the SDF rather than running the direct simulation without data assimilation even when the initial condition is accurately known – since there is no initial condition uncertainty in the discretization error. We also point out that – despite the fact that the linearized filter involves normal displacements – the results obtained in this nonlinear case are much better than in the linear case with normal displacements. This can be interpreted by the fact that the motion of the normal vectors $\underline{\nu}_{S_k}$ significantly enhances observability compared to the fixed normals considered in the purely Lagrangian linear estimator of Section 3.5.

5 Extension to Nonlinear Mechanics

The above estimation strategy can be extended with ease to nonlinear mechanical systems as follows. We generalize the system discussed in Section 2 by considering:

- a hyperelastic material given by the Ciarlet-Geymonat potential

$$W^e(\underline{\underline{e}}) = \kappa_1(J_1 - 3) + \kappa_2(J_2 - 3) + \kappa_3(J - 1) - \kappa_3 \ln J,$$

  where $\underline{\underline{e}}$ denotes the nonlinear Green-Lagrange strain tensor and J_1, J_2, J the classical reduced invariants, see e.g. [12].

- a viscous term corresponding to the pseudopotential

$$W^v(\underline{\underline{e}}) = \beta\, Tr(\dot{\underline{\underline{e}}}^2).$$

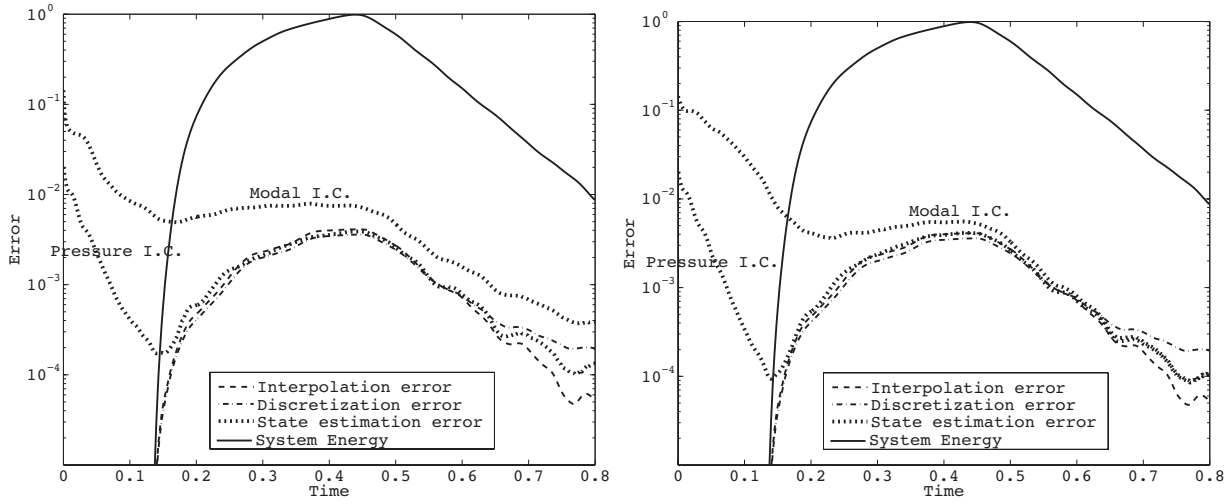

Figure 14: Estimation errors with segmented images: DDF (left) and SDF (right)

- a prestress term

$$\delta\mathcal{W}^{PS} = \int_\Omega \sigma_0 w(\|\underline{CM}\| - ct)\ \mathrm{Tr}(\delta\underline{e})\, d\Omega.$$

In the numerical simulations we have used the values

$$\kappa_1 = 2.2\,10^3\,\mathrm{Pa}, \quad \kappa_2 = 33\,\mathrm{Pa}, \quad \kappa_3 = 2\,10^4\,\mathrm{Pa}, \quad \beta = 0.68\,\mathrm{Pa.s}, \tag{47}$$

which give the same linearized dynamics as above in the small displacement framework.

This nonlinear setting leads to a discrete system in the form

$$\begin{cases} \dot{X}^d = X^v \\ M\dot{X}^v + C(X^d)X^v + F^{\mathrm{int}}(X^d) = F^{PS}(X^d, t) \end{cases} \tag{48}$$

where $F^{int}(X^d)$ denotes the internal force vector derived from the hyperelastic potential, $C(X^d)X^v$ the viscous force vector, and $F^{PS}(X^d, t)$ the prestress force vector.

We then propose as an estimator the following system

$$\begin{cases} K(\hat{X}^d, \hat{X}^v)\dot{\hat{X}}^d = K(\hat{X}^d, \hat{X}^v)\hat{X}^v + \gamma(H^d)'(Z - H^d\hat{X}^d) \\ M\dot{\hat{X}}^v + C(\hat{X}^d)\hat{X}^v + F^{\mathrm{int}}(\hat{X}^d) = F^{PS}(\hat{X}^d, t) \end{cases} \tag{49}$$

where $K(\hat{X}^d)$ denotes the tangent stiffness operator matrix of the mechanical system, namely,

$$K(\hat{X}^d, \hat{X}^v) = \frac{\partial}{\partial Y}(F^{\mathrm{int}} - F^{PS})(\hat{X}^d) + \frac{\partial C}{\partial Y}(\hat{X}^d).\hat{X}^v.$$

The linearized error arround the true dynamics then obeys

$$\begin{cases} K(X^d, X^v)\dot{\tilde{X}}^d = K(X^d)\tilde{X}^v - \gamma(H^d)'H^d\tilde{X}^d - \gamma(H^d)'(\epsilon_h + \chi) \\ M\dot{\tilde{X}}^v + C(X^d)\tilde{X}^v + K(X^d, X^v)\tilde{X}^d = 0 \end{cases} \tag{50}$$

Although K and C are now time-dependent, the dynamics of the linearized error remains stabilized simply because the same argument as for the linear dynamics holds as long as $K(X^d, X^v)$ remains

positive. Using classical stability results for nonautonomous nonlinear systems (see e.g. [10]), this ensures that there exists a neighborhood of 0 for the initial error $\tilde{X}(0) = \zeta_X$ in which the error dynamics is stable. We emphasize that – in the SDF filter – it is now $K(\hat{X}^d, \hat{X}^v)$ which is used in the definition of the adjoint operator $(H^d)'$.

We show in Figure 15 the SDF numerical estimation results obtained for a pressure filling initial condition, for a pressure value increased by a factor 1.8 with respect to our previous simulations in order to assess the effectiveness and the robustness of the filter. We can see that – even for a nonlinear mechanical system with large initial condition errors – the performance of the SDF filter is excellent. In the estimation error curves we also plot the results obtained when using the fixed stiffness matrix $K(X^d(0), 0)$ – namely, the same as in the linear case – instead of $K(\hat{X}^d, \hat{X}^v)$ in the filter. The very close similarity observed between the estimation results can be interpreted by the fact that – in the linearized error system (50) – the tangent stiffness operator $K(X^d, X^v)$ remains fixed at the initial (undeformed) value until the system is activated, by which time the estimator already approximates the true system with excellent accuracy.

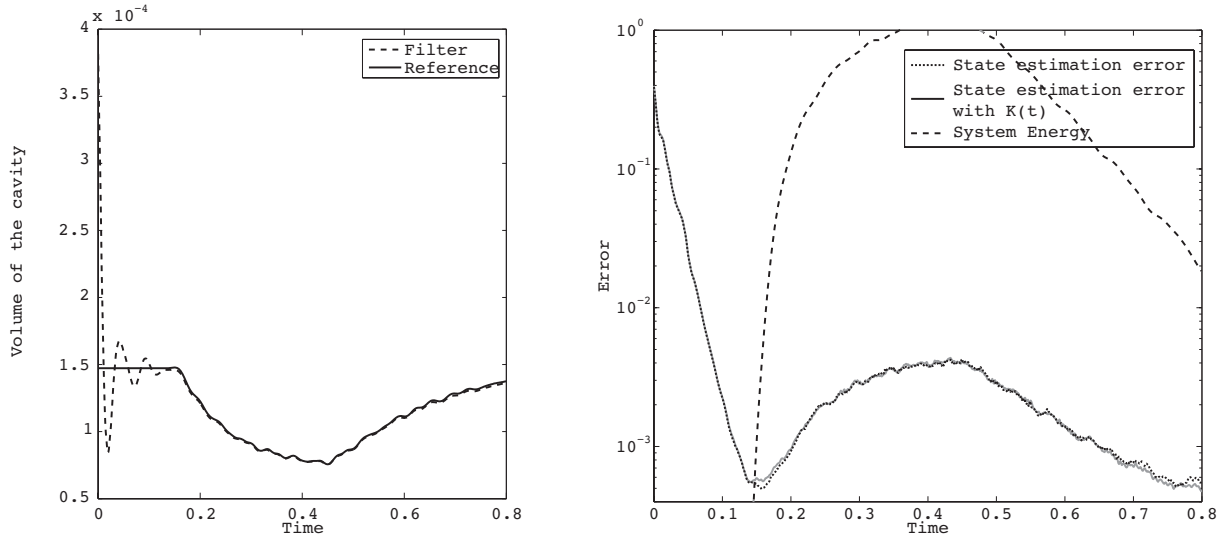

Figure 15: Estimated volume (left) and estimation error (right) for nonlinear system

6 Concluding remarks

We have proposed a new filtering methodology to perform estimation on a distributed mechanical system, using a filter inspired from feedback control, which gives an effective and robust procedure with computations of the same order of complexity as direct numerical simulations of the system. We depart from our previous work in that – since we do not need to apply the control on a real system but only in the purely numerical estimator – we use a correction term in the dynamical equation relating position and velocity, which allows to employ position measurements instead of velocity. Furthermore, using a lifting of the observed part of the state – via a Schur complement method – we can achieve the same level of performance as with velocity measurements by applying the stiffness operator on the lifting in the filter. This was substantiated by an analysis of the estimation system, and further demonstrated by numerical assessments using a test problem inspired from cardiac biomechanics. We have also shown how our methodology can be extended – with ease and similar performances – to cover nonlinear observation operators, as when considering segmented

images. An extension to nonlinear mechanical systems has also been proposed and successfully assessed.

We point out that our control-based estimation approach is not restricted to mechanical systems and could – indeed – be extended in principle to any other system modeled by evolution PDEs for which effective feedback strategies are available or could be further developed by fully exploiting the estimation system without any constraint on the applicability of the control on a real system.

Although we have not discussed parametric estimation, extending the state estimator presented in the present work to perform joint state-parameter estimation is quite straightforward by following the methodologies proposed in [6, 14].

As regards the type of observation operator considered for image measurements, other choices could be made, e.g. starting from 3D-distributed image norms – instead of surface distances – commonly used in image processing procedures, see [16] and references therein. This will require some further investigation, in particular as to the well-posedness of the filter that requires adequate differentiability properties for the norm in question.

Finally, further work must be performed to evaluate the effectiveness of the proposed methodology when using *real imaging measurements*. Of course, modeling errors will then be an additional difficulty to cope with, but the estimation procedure can also be used as a tool to assess model validity, since its success – now that it has been validated with synthetic data – would thus only depend on model adequacy.

References

[1] E. Angelini and O. Gérard. Review of myocardial motion estimation methods from optical flow tracking on ultrasound data. In *Proc. of the 28th IEEE EMBS Annual International Conference*, 2006.

[2] N. Ayache, editor. *Computational Models for the Human Body*. Handbook of Numerical Analysis (Ph. Ciarlet series editor). Elsevier, 2004. 670 pages.

[3] J. Baerentzen and H. Aanaes. Signed distance computation using the angle weighted pseudo-normal. *IEEE Transactions on Visualization and Computer Graphics*, 11(3):243–253, may 2005.

[4] K.J. Bathe. *Finite Element Procedures*. Prentice Hall, 1996.

[5] A. Bensoussan. *Filtrage Optimal des Systèmes Linéaires*. Dunod, 1971.

[6] D. Chapelle, P. Moireau, and P. Le Tallec. Robust filtering for joint state-parameter estimation in distributed mechanical systems. *DCDS-B*, in press, 2008.

[7] I. Cohen, L.D. Cohen, and N. Ayache. Using deformable surfaces to segment 3-D images and infer differential structures. *Image Understanding*, 53(2):211–218, 1991.

[8] J. Declerck, T. Denney, C. Oztürk, W. O'Dell, and E.R. McVeigh. Lv motion reconstruction from tagged MRI: a comparison. In *International Society of Magnetic Resonance in Medicine*, page 1283, Philadelphia, PA, USA, May 1999.

[9] S. Ervedoza and E. Zuazua. Uniformly exponentially stable approximations for a class of damped systems. To be published in Journal de Mathématiques Pures et Appliquées, 2008.

[10] W. Hahn. *Stability of Motion*. Springer Verlag, 1967.

[11] T.J.R. Hughes. *The Finite Element Method : Linear Static and Dynamic Finite Element Analysis*. Prentice Hall, 1987.

[12] P. Le Tallec. *Handbook of Numerical Analysis*, volume 3, chapter Numerical Methods for Nonlinear Three-dimensional Elasticity. North-Holland, 1994.

[13] D.G Luenberger. An introduction to observers. *IEEE Transactions on Automatic Control*, 16:596–602, 1971.

[14] P. Moireau, D. Chapelle, and P. Le Tallec. Joint state and parameter estimation for distributed mechanical systems. *Computer Methods in Applied Mechanics and Engineering*, 197:659–677, 2008.

[15] A. Montillo, D.N. Metaxas, and L. Axel. Automated segmentation of the left and right ventricles in 4D cardiac SPAMM images. In *MICCAI '02: Proceedings of the 5th International Conference on Medical Image Computing and Computer-Assisted Intervention-Part I*, pages 620–633, London, UK, 2002. Springer-Verlag.

[16] J.M. Morel and S. Solimini. *Variational Methods in Image Segmentation*. Birkhauser, 1993.

[17] X. Papademetris, A. J. Sinusas, D. P. Dione, and J. S. Duncan. Estimation of 3D left ventricular deformation from echocardiography. *Medical Image Analysis*, 8:285–294, 2004.

[18] D.T. Pham, J. Verron, and M.C. Roubeaud. A singular evolutive interpolated kalman filter for data assimilation in oceanography. *J. Marine Systems*, 16:323–341, 1997.

[19] A. Preumont. *Vibration Control of Active Structures, An Introduction*. Kluwer Academic Publishers, 2nd edition, February 2002.

[20] J. Sainte-Marie, D. Chapelle, R. Cimrman, and M. Sorine. Modeling and estimation of the cardiac electromechanical activity. *Computers & Structures*, 84:1743–1759, 2006.

[21] M. Sermesant, C. Forest, X. Pennec, H. Delingette, and N. Ayache. Deformable biomechanical models: Application to 4D cardiac image analysis. *Medical Image Analysis*, 7(4):475–488, December 2003. PMID: 14561552.

[22] M. Sermesant, P. Moireau, O. Camara, J. Sainte-Marie, R. Andriantsimiavona, R. Cimrman, D. L. Hill, D. Chapelle, and R. Razavi. Cardiac function estimation from MRI using a heart model and data assimilation: Advances and difficulties. *Medical Image Analysis*, 10(4):642–656, 2006.

[23] F. Tisseur and K. Meerbergen. The quadratic eigenvalue problem. *SIAM Review*, 43(2):235–286, 2001.

[24] A. Toselli and O. Widlund. *Domain decomposition methods—algorithms and theory*, volume 34 of *Springer Series in Computational Mathematics*. Springer-Verlag, Berlin, 2005.

[25] J. von Berg, H. Barschdorf, T. Blaffert, S. Kabus, and C. Lorenz. Surface based cardiac and respiratory motion extraction for pulmonary structures from multi-phase ct. In A. Manduca and X.P. Hu, editors, *Medical Imaging 2007: Physiology, Function, and Structure from Medical Images*, volume 6511, page 65110Y. SPIE, 2007.